# Strong reflector-based beamforming in ultrasound medical imaging

Teodora Szasz, Adrian Basarab, Denis Kouamé

**To cite this version:**

Teodora Szasz, Adrian Basarab, Denis Kouamé. Strong reflector-based beamforming in ultrasound medical imaging. Ultrasonics, 2016, 66, pp.111-124. 10.1016/j.ultras.2015.11.003 . hal-01567077

**HAL Id: hal-01567077**

**https://hal.science/hal-01567077v1**

Submitted on 21 Jul 2017

**To link to this article** : DOI : 10.1016/j.ultras.2015.11.003
URL : https://doi.org/10.1016/j.ultras.2015.11.003

**To cite this version** : Szasz, Teodora and Basarab, Adrian and Kouamé, Denis *Strong reflector-based beamforming in ultrasound medical imaging.* (2016) Ultrasonics, vol. 66. pp. 111-124. ISSN 0041-624X

# Strong reflector-based beamforming in ultrasound medical imaging

Teodora Szasz [*], Adrian Basarab, Denis Kouamé

*Université de Toulouse, IRIT, UMR CNRS 5505, France*

## ABSTRACT

This paper investigates the use of sparse priors in creating original two-dimensional beamforming methods for ultrasound imaging. The proposed approaches detect the strong reflectors from the scanned medium based on the well known Bayesian Information Criteria used in statistical modeling. Moreover, they allow a parametric selection of the level of speckle in the final beamformed image. These methods are applied on simulated data and on recorded experimental data. Their performance is evaluated considering the standard image quality metrics: contrast ratio (CR), contrast-to-noise ratio (CNR) and signal-to-noise ratio (SNR). A comparison is made with the classical delay-and-sum and minimum variance beamforming methods to confirm the ability of the proposed methods to precisely detect the number and the position of the strong reflectors in a sparse medium and to accurately reduce the speckle and highly enhance the contrast in a non-sparse medium.

We confirm that our methods improve the contrast of the final image for both simulated and experimental data. In all experiments, the proposed approaches tend to preserve the speckle, which can be of major interest in clinical examinations, as it can contain useful information. In sparse mediums we achieve a highly improvement in contrast compared with the classical methods.

*Keywords:*
Adaptive beamforming
Sparse signal representation
Ultrasound imaging
Bayesian Information Criteria

## 1. Introduction

Ultrasound (US) imaging is one of the most commonly used medical imaging modalities. Its low-cost, non-ionizing characteristics, ease-of-use and real-time nature makes it the gold standard for many crucial diagnostic exams, especially in obstetrics and cardiology.

Beamforming (BF) or spatial filtering [1] enables the selectivity of the acoustic signals reflected from some known positions, while attenuating the signals from other positions. This is classically done by delaying and applying some specific weights to the reflected signals. The applications of BF are versatile to many areas: radar, sonar, imaging, communications, radio astronomy and others. The beamformers can be either data-independent (fixed), or data-dependent (adaptive), depending on the calculation of the weights applied to the output array of the reflected signals. The simplest yet most used data-independent BF method in US imaging is the classical delay-and-sum (DAS) BF, which uses fixed apodization weights to approximate the array response independent of the array data. Unfortunately, the resolution and the contrast achievable with DAS are limited. On the other hand, the adaptive beamformers calculate the weights from the statistics of the received data in order to converge to an optimal response. Thus, the contributions of the noise and the signals that arrive from other directions than the desired one are minimized.

The data-dependent beamformers offer a better resolution and a higher interference rejection capability if the signal of interest (SOI) and the true covariance matrix are accurately known. Different data-dependent approaches may be found in literature. Capon introduced the widely used Capon or minimum variance (MV) beamformer [2], which minimizes the power of the weighted array data such that the desired signal passes without distortion. However, in practice, just an estimation of the covariance matrix can be provided, which can be ill-conditioned, providing worst results than the fixed BF methods. In consequence, more robust adaptive beamformers have been developed. Bell et al. [3] proposed a Bayesian approach, robust to uncertainty of the direction of arrival (DOA) of the source. More recently, Li and Stoica proposed a spherical set constrained on the beamformer steering vector, using also the popular diagonal loading approach for improving the robustness of the Capon beamformer [4].

In medical US imaging, Asl et al. combined MV with diagonal loading and phase coherence factor (see e.g. [5,6]) to achieve better results than DAS in terms of lateral resolution, sidelobes reduction and contrast. Another approach proposed by Holfort et al. uses frequency subbands and calculates a set of complex apodization weights for each frequency subband [7]. They argue an increase of contrast and lateral resolution even in the case of plane-wave

---

[*] Corresponding author.

US imaging (when only one emission is used). Recently, Diamantis et al. provide a comparison between the temporal and frequency subband approaches of MV for US images and show that there are insignificant differences in terms of spatial resolution and contrast [8]. Moreover, Rindal et al. contest the improvement in contrast related to MV, and show that this is the result of the increase in lateral resolution [9].

A new perspective in adaptive BF was recently exploited, based on sparse representation of the signals. Yartibi et al. proposed two user parameter-free BF approaches for estimating source locations in array processing: the iterative adaptive approach (IAA) and the maximum likelihood based IAA (IAA-ML) [10,11]. These methods take as input the result of DAS and, using an iterative algorithm, minimize the weighted least squares (WLS) cost function in order to estimate the signal powers.

Sparse modeling gained a special interest in medical US, as for example in modeling the amplitude of the potential reflectors by using an iterative adaptive approach (IAA) present in array processing literature [12]. Other examples can be the applications that concern compressive sensing [13]. Tur et al. model the echoes reflected by multiple reflectors located at unknown positions in the medium, as a sum of a small number of pulses with known shapes [14]. Based on this, Wagner et al. proposed a two-dimensional reconstruction method for US imaging, called "compressed beamforming" [15]. They used multiple array elements in receive and beamformed the sub-Nyquist received samples.

In our preliminary work [16], we obtained a sparse signal representation by extending the DAS BF method with BIC (Bayesian Information Criteria) selection criteria. Here, we improve the previously proposed method in order to obtain more realistic results in terms of speckle conservation. Moreover, we extend MV BF method with BIC in order to exploit the advantages of the MV BF to our sparse modeling. Finally, we propose a new method that computes the final beamformed image by combining the sparse representation with the DAS and MV beamformed results. Compared with DAS and MV, we increase the contrast while preserving the speckle (that frequently contain important clinical information) in the final beamformed image.

The reminder of this paper is as follows: in Section 2 we describe the background of DAS and MV BF method. In Section 3 we present the proposed method that was validated both on pulse echo simulated ultrasound data and real ultrasound phantom data recorded with an Ultrasonix MDP scanner. A detailed description of the experiments is given in Section 4. Section 5 presents the results and Section 6 concludes the paper.

## 2. Background on US beamforming

Throughout this paper, we denote the vectors and the matrices with boldface lowercase, respectively with boldface capital letters. In Table 1 we describe the notations used in this paper.

The basic principle of US imaging consists in emitting US waves with a probe towards a target medium and receiving the reflected (or backscattered) waves (echoes) resulting from the interaction between US waves and the tissues. These acquired signals (raw data) are delayed, weighted using apodizations and summed to obtain the radio-frequency (RF) signals. The most used method to display an US image is the B-mode and consists in extracting the envelope of the RF signals, filtering and log-compressing.

**Table 1**
Mathematical notations used in the paper.

| Notation | Explanation |
|---|---|
| $M$ | Number of elements of the probe |
| $M_{act}$ | Number of active elements in emission and reception |
| $N$ | Number of samples of each RF signal |
| $\boldsymbol{Y}^{(i)}$ | Raw data of size $M_{act} \times N$ corresponding to the $i$th pulse emission |
| $\boldsymbol{Y}_d^{(i)}$ | Dynamically focused raw data of size $M_{act} \times N$ corresponding to the $i$th pulse emission |
| $\boldsymbol{w}$ | Beamformer weight vector of size $1 \times M_{act}$ |
| $\boldsymbol{w_h}$ | Hanning window of size $1 \times M_{act}$ |
| $\boldsymbol{R}$ | Covariance matrix |
| $\hat{\boldsymbol{R}}$ | Estimated covariance matrix |
| $\boldsymbol{y}_k^{(i)}$ | Non-focused raw signal of size $1 \times N$ received by the $k$-th element, corresponding to emission $k$ |
| $\boldsymbol{y}_d^{(i)}$ | Focused raw signal of size $1 \times N$ |
| $\hat{\boldsymbol{S}}$ | DAS beamformed image of size $M \times N$ |
| $\hat{\boldsymbol{s}}_i$ | $i$th DAS beamformed RF signal of size $1 \times N$ |
| $\tilde{\boldsymbol{S}}$ | MV beamformed image of size $M \times N$ |
| $\tilde{\boldsymbol{s}}_i$ | $i$th MV beamformed RF signal of size $1 \times N$ |
| $\boldsymbol{s}_i$ | USBIC or M-USBIC beamformed RF signal |
| $\boldsymbol{S}^{(K)}$ | USBIC or M-USBIC sparse beamformed image |
| $\boldsymbol{S}_{USBIC}$ | Final USBIC beamformed image with speckle |
| $\boldsymbol{S}_{M-USBIC}$ | Final M-USBIC beamformed image with speckle |
| $\lambda$ | Parameter for setting the sparsity level |
| $\gamma$ | Parameter for setting the speckle level |
| $(\cdot)^T$ | Transpose of a vector or matrix |
| $(\cdot)^H$ | Conjugate transpose of a vector or matrix |
| $\circ$ | Hadamard product of two vectors/matrices |
| $f_{1D}(k)$ | Cost function for 1D BIC approach |
| $f_{2D}(k)$ | Cost function for 2D BIC approach |
| $\Vert \cdot \Vert_2$ | $l_2$-norm |
| $\mathbf{1}^\top$ | Is the transpose of a all-ones matrix |
| $K$ | Number of strong reflectors |

Assuming an $M$-element ultrasound probe, we consider hereafter the classical acquisition scheme, where a series of focused beams is transmitted with $M_{act}$ elements. The raw signals are recorded using the same subarray that was used for transmission. The DAS beamformed RF signals can be written as:

$$\hat{\boldsymbol{s}}_i(n) = \boldsymbol{w}^H(n)\boldsymbol{y}_d^{(i)}(n) = \sum_{k=1}^{M_{act}} w_k(n)\boldsymbol{y}_k^{(i)}(n - \Delta_k(n)) \quad n = 1, \ldots, N, \tag{1}$$

where $N$ is the number of samples of the RF signal, $\boldsymbol{y}_k^{(i)}$ is the $1 \times N$ raw data received by the $k$-th element of the ultrasound probe corresponding to emission number $(i), \Delta_k(n)$ is the time delay dependent on the distance between the $k$-th element and the point of interest in the image, $w_k$ are the beamformer weights, $\boldsymbol{y}_d^{(i)}(n) \in \mathbb{R}^{M_{act}\times 1}$, $\boldsymbol{y}_d^{(i)}(n) = \boldsymbol{y}^{(i)}(n - \Delta_k(n))$ is the dynamically focused version of the raw data $\boldsymbol{y}^{(i)}(n) = [y_1^{(i)}(n), \ldots, y_{M_{act}}^{(i)}(n)]^T$, $\boldsymbol{w}(n) = [w_1, \ldots, w_{M_{act}}]^T$ is the vector of the beamformer weights, $(\cdot)^T$ and $(\cdot)^H$ represent the transpose and conjugate transpose, respectively. Without loss of generality, for simplicity purpose, we consider throughout the theoretical part that the number of the beamformed RF lines is equal to $M$.

While the DAS beamformer uses fixed data-independent weights $\boldsymbol{w}$, the aim of MV is to apply an optimal set of weights in order to estimate the desired signal waveform as accurately as possible, while rejecting the interfering signals. The optimal weights in the sense of MV, can be obtained from the expression of the signal-to-interference-plus-noise ratio ($SINR$) [17]:

$$SINR = \frac{\sigma_s^2 |\boldsymbol{w}^H \boldsymbol{a}|^2}{\boldsymbol{w}^H \boldsymbol{R} \boldsymbol{w}}, \tag{2}$$

where $\boldsymbol{R}$ of size $M_{act} \times M_{act}$ is the interference-plus-noise covariance matrix, $\sigma_s^2$ is the signal power and $\boldsymbol{a}$ the steering vector. To have a maximum $SINR$, the output interference-plus-noise power is minimized, while maintaining a distortionless response to the desired signal:

$$\min_{\boldsymbol{w}} \ \boldsymbol{w}^H \boldsymbol{R} \boldsymbol{w}, \ \text{subject to } \boldsymbol{w}^H \boldsymbol{a} = 1. \tag{3}$$

After applying the proper delays to the raw data, $\boldsymbol{a}$ becomes a vector of ones. Therefore, the solution of (3), also called the minimum variance distortionless response beamformer ($\boldsymbol{a}$ is the steering vector across the array), is:

$$\tilde{\boldsymbol{w}} = \frac{\boldsymbol{R}^{-1}\boldsymbol{a}}{\boldsymbol{a}^H\boldsymbol{R}^{-1}\boldsymbol{a}}. \tag{4}$$

As in practical situation the analytical form of $\boldsymbol{R}$ is not known, it is usually replaced by the estimated covariance matrix derived from $P$ received samples, denoted by $\hat{\boldsymbol{R}}$:

$$\hat{\boldsymbol{R}} = \frac{1}{P}\sum_{p=1}^{P}\boldsymbol{y}_d^{(i)}(p)\boldsymbol{y}_d^{(i)}(p)^H. \tag{5}$$

In order to decorrelate the coherent signals received from the $M_{act}$ elements, the subarray-averaging method is generally used. Specifically, the $M_{act}$ element linear array is divided into $M_{act} - L + 1$ overlapping subarrays of size $L$, and the covariance matrices from $L$ subarrays are averaged [18]. However, it was shown that in this case the tissue may appear less homogeneous and may give different statistics compared with DAS [19]. To retain the speckle statistics, the temporal averaging was introduced in [20]. By averaging both in the spatial (lateral direction) and temporal domains, the resolution can be further improved, with no contrast degradation. Finally, the MV beamformer output can be expressed as:

$$\tilde{s}_i(n) = \frac{1}{M_{act} - L + 1}\sum_{l=1}^{M_{act}-L+1}\tilde{\boldsymbol{w}}^H(n)\boldsymbol{y}_d^{(i)(l)}(n), \quad i = 1,\dots,M, \tag{6}$$

where $\boldsymbol{y}_d^{(i)(l)}(n)$ is the dynamically focused raw data corresponding to the $l$-th subarray of size $L$.

## 3. Beamforming with sparse priors: proposed method

Based on the beamforming methods reviewed in the previous section (DAS and MV), the proposed method consists in detecting and reinforcing the strong reflectors in the RF images. In practice, these reflectors may be associated to the tissue boundaries or the small hyperechoic structures (see e.g. [14,15]).

As we will explain below, the strong reflector detection is based on the minimization of the Bayesian Information Criteria (BIC), balancing between data fidelity and a sparsity-based penalization term [21].

### 3.1. Sparse strong reflector model

The strong reflector model of an RF image $\boldsymbol{S}$, considered herein as a collection of $M$ RF lines each one having $N$ samples, is given as:

$$\begin{aligned}&\boldsymbol{S}(x,n) = \sum_{k=1}^{K} a_k \boldsymbol{h}_k(x - x_k, n - n_k),\\ &x = x_1,\dots,x_M \quad \text{and} \quad n = 1,\dots,N,\end{aligned} \tag{7}$$

where $n$ stands for the time or axial (longitudinal) direction, $x$ is the lateral direction variable, and $\boldsymbol{S}(x,n)$ is the beamformed RF image. $(x_k, n_k)$, with $k = 1,\dots,K$ are the positions of the $K$ strong reflectors to be detected during the proposed beamforming process. We denote with $a_k$ the amplitudes of the strong reflectors and with $\boldsymbol{h}_k(x,n)$ the backscattered pulse corresponding to the strong reflector $k$, both supposed unknown and to be estimated. In this case the term sparsity is related to the relatively low number of strong reflectors to be detected by the proposed method.

### 3.2. Strong reflector detection and parameter estimation

In this section, we describe the proposed process of strong reflector detection and parameter estimation. The proposed method is mainly divided in two steps: the detection step, based on the previously beamformed RF lines, finds the strong reflectors taking into account the amplitudes of the RF signals. Then, the validation step uses the raw data to confirm the previously detected reflectors through the BIC criteria. The main reason of processing the detection of the strong reflectors on beamformed data instead of raw data is related to the SNR that is naturally higher on standardly beamformed data compared to raw data. Thus, we expect that the results are less affected by the low SNR when detecting the peaks on DAS or MV images.

For the ease of understanding, we use the same notations as in Section 2, corresponding to a classical pulse echo US image. The raw data is collected with the corresponding $M_{act}$ active elements, resulting into a data matrix of size $M_{act} \times N$, denoted by $\boldsymbol{Y}_d^{(i)}$. More precisely, $\boldsymbol{y}_d^{(i)}(n)$ is a $M_{act} \times 1$ line corresponding to emission number $(i)$ and to depth $n$, after the dynamic focalisation of the received echoes.

As explained in Section 2, the total amount of raw data is used in non-adaptive BF process to obtain the DAS beamformed RF image denoted by $\hat{\boldsymbol{S}}$, or in an adaptive BF process to form the MV beamformed RF image denoted by $\tilde{\boldsymbol{S}}$. We denote $\hat{\boldsymbol{s}}_i$, and $\tilde{\boldsymbol{s}}_i$ the $i$th RF signals extracted from $\hat{\boldsymbol{S}}$, respectively $\tilde{\boldsymbol{S}}$. Our strong reflector detection and parameter estimation method uses both the raw data $\boldsymbol{Y}_d^{(i)}$, and the beamformed RF images $\hat{\boldsymbol{S}}$ or $\tilde{\boldsymbol{S}}$. Both proposed approaches, using the DAS or MV beamformed RF images, are similar and will be referred as USBIC, respectively M-USBIC in the reminder of the paper.

Two main steps are used within the proposed method. The first step uses $\hat{\boldsymbol{S}}$ or $\tilde{\boldsymbol{S}}$ to detect a potential strong reflector (its position, amplitude, and pulse response). The second step validates this choice and estimation based on a cost function implying the raw data. The first and the second steps are alternatively repeated until the algorithm stops (the minimum of BIC is reached). Moreover, an initial one-dimensional (1D) approach is followed by a two-dimensional (2D) refinement, both using the two aforementioned steps. In the following, we describe only the steps required to form the USBIC beamformed RF image (denoted with $\boldsymbol{S}^{(K)}$ in the paper). In this case we use as input the DAS beamformed RF image $\hat{\boldsymbol{S}}$, and the raw data $\boldsymbol{Y}_d^{(i)}$. The steps to form the M-USBIC beamformed RF image (when the MV beamformed RF image $\tilde{\boldsymbol{S}}$ and the $\boldsymbol{Y}_d^{(i)}$ are the inputs) are identical with the ones required to form USBIC beamformed RF image.

#### 3.2.1. 1D initialization procedure

For each beamformed RF line $\hat{\boldsymbol{s}}_i$ at lateral position $x_i$ the strong reflector detection and validation are iterated. For iteration $k$, the two steps are process as follows:

*Step 1 – Strong reflector detection.*

$$\begin{aligned}&n_k = \underset{n\backslash\{n_1,\dots,n_{k-1}\}}{\operatorname{argmax}}\,(|\hat{\boldsymbol{s}}_i(n)|),\\ &a_k = |\hat{\boldsymbol{s}}_i(n_k)|,\\ &\boldsymbol{h}_k(x_i,n) = \hat{\boldsymbol{S}}(x_i,n)\circ\boldsymbol{w}_{\boldsymbol{h}}(n),\\ &\quad n = \left[n_k - \frac{\tau_{pulse}\cdot f_s}{2},\dots,n_k + \frac{\tau_{pulse}\cdot f_s}{2}\right],\end{aligned} \tag{8}$$

where $n_k$ is in the interval $\{1,\dots,N\}$, $\hat{\boldsymbol{S}}(x_i,n)$ is the DAS beamformed image, $\boldsymbol{w}_{\boldsymbol{h}}$ is a Hanning window, $\tau_{pulse}$ is the predefined pulse length (equal to twice the excitation length in this paper), $f_s$

is the sampling frequency, $\circ$ defines the Hadamard product, and argmax stands for the argument of the maximum. The current form of the detected strong reflector RF signal, after $k$ iterations, is:

$$\boldsymbol{s}_{\boldsymbol{i}}^{(k)} \triangleq \boldsymbol{S}^{(k)}(x_i, n) = \sum_{p=1}^{k} a_p \boldsymbol{h}_p(x_i, n), \tag{9}$$

where $\boldsymbol{s}_{\boldsymbol{i}}^{(k)}$ is the $i$-th column of the RF image $\boldsymbol{S}^{(k)}(x, n)$, at the iteration $k$.

*Step 2 – Validation.* In the second step of each iteration, a cost function is calculated balancing between on the one hand, the data fidelity between the current RF model in (9) and the raw data and on the other hand, the sparsity of the strong reflectors. The BIC evaluation criterion [21] is one of the most used information criteria in statistics, having the role of assessing the closeness between the predictive distribution defined by a statistical model and the true distribution. A statistical model uses the observed data to approximate the true distribution of certain probabilistic events. Let $g(\upsilon_n|\hat{\theta})$ be a statistical model estimated by the maximum likelihood method. Than, the BIC criterion is defined as:

$$BIC(n) = -2\log g(\upsilon_n|\hat{\theta}) + p\log n, \tag{10}$$

where $\theta$ is the unknown parameter, $\hat{\theta}$ is its estimator, and $\upsilon_n$ are the observations, $\upsilon_n = \{\upsilon_1, \upsilon_2, \ldots, \upsilon_n\}$. Inspired from the application of BIC with IAA for obtaining sparsity by estimating the number of sources in array processing, described in [11], BIC was adapted herein to US imaging. The cost function $f_{1D}(k)$ has the following form:

$$f_{1D}(k) = \overbrace{\log(\|\boldsymbol{s}_{\boldsymbol{i}}^{(k)} \cdot \boldsymbol{1}^{\top} - \boldsymbol{y}_d^{(i)}\|_2^2)}^{\text{data fidelity}} + \underbrace{\lambda k \log(N)}_{\text{sparsity constraint}}, \tag{11}$$

where $\lambda$ is an user-defined parameter fixing the compromise between the data attachment and the sparsity. Even if the automatic choice of the $\lambda$ is out of the scope of this paper, note that there exist in literature several approaches that automatically determine the value of this kind of hyperparameter, see e.g. [22–25].

For each RF line, *Step 1* and *Step 2* are iterated until the cost function in (11) starts to increase (i.e. $f_{1D}(k+1) > f_{1D}(k)$). Note that the data fidelity term is not related to already beamformed RF lines, but to the raw data (native data received by each element of the US probe), at each iteration, having the dimension $M_{act} \times N$.

Let us denote by $\Psi$ the set of all the strong reflector positions detected from all individual RF lines. Applied on each RF line, the algorithm tends to overestimate the number of strong reflectors. Moreover and more important, it does not ensure a spatial coherence between the neighboring RF lines. For this reason, a 2D approach follows the 1D method, and is presented bellow. It will choose a subset of strong reflectors of $\Psi$ respecting a 2D BIC criteria. The main advantage of applying the 1D approach is to speed up (at least three times in our experiments) the 2D process that will have as input just the potential strong reflectors detected previously by the 1D method for each RF line.

#### 3.2.2. 2D refinement procedure

For the refinement of the previously detected reflectors (by the 1D approach) we use the set $\Psi$, representing all the strong reflectors positions of all the RF lines. For all strong reflectors detected in the 1D approach, an 2D – adapted BIC criteria is applied. The process of the 2D refinement iteratively gathers the best positions from the set $\Psi$, as follows:

$$n_k = \underset{n \in \Psi \setminus \{n_1, \ldots, n_{k-1}\}}{\operatorname{argmax}} (a_n), \tag{12}$$

where $a_n$ is expressed in (8). The selected strong reflectors are plugged into the 2D BIC criteria, given by:

$$f_{2D}(k) = \overbrace{\log\left(\sum_{i=1}^{M} \|\boldsymbol{s}_{\boldsymbol{i}}^{(k)} \cdot \boldsymbol{1}^{\top} - \boldsymbol{y}_d^{(i)}\|_2^2\right)}^{\text{data fidelity}} + \underbrace{\lambda k \log(N)}_{\text{sparsity constraint}}, \tag{13}$$

where $\boldsymbol{s}_{\boldsymbol{i}}^{(k)}$ is defined in (9).

The 2D validation step is iterated until the function $f_{2D}(k)$ starts to increase, similar as for the *1D initialization approach*. Moreover, as stated in Section 3.2.1, the data fidelity term for the 2D approach is composed of all the focused raw data corresponding to all emissions, having the dimension $M_{act} \times M \times N$.

### 3.3. Final image computation

As we will show in the results section, the method introduced in Section 3.2 has a good ability to detect the strong reflectors and to provide a sparse version of the RF image. However, it does not preserve the speckle characteristics, that can contain clinical information, in the case when the examined medium is not sparse. For this reason, we propose to further combine our sparse RF image with the one that is classically beamformed with DAS or MV, as shown below. If the DAS RF image $\widehat{\boldsymbol{S}}$ is used (for strong reflector detection and final image combination), we call the resulted image USBIC. If the MV RF image $\widetilde{\boldsymbol{S}}$ is used, we call it M-USBIC. Hence, the final USBIC beamformed image can be expressed as:

$$\boldsymbol{S}_{USBIC} = \gamma \cdot \widehat{\boldsymbol{S}} + (1-\gamma) \cdot \boldsymbol{S}^{(K)}, \tag{14}$$

where $\boldsymbol{S}^{(K)}$ is the beamformed image obtained using our sparse strong reflector model and is defined in (7), $\gamma$ is the parameter that control the level of speckle in the final image, and $K$ is the number of the strong reflectors detected after the $k$ iterations.

Similar, the M-USBIC has the following expression:

$$\boldsymbol{S}_{M-USBIC} = \gamma \cdot \widetilde{\boldsymbol{S}} + (1-\gamma) \cdot \boldsymbol{S}^{(K)} \tag{15}$$

Note that $\boldsymbol{S}^{(K)}$ be obtained either by using the DAS beamformed image (in the case of USBIC, or starting from the MV beamformed image (in the case of M-USBIC).

## 4. Experiments

In order to evaluate the proposed USBIC and M-USBIC BF approaches, we have considered three different simulated examples using the Field II simulation program [26] and one recorded ultrasound phantom data. The first simulated medium is based on a sparse assumption of the reflectors. The second one is based on simulated data from scenes of point-targets and scenes of cysts in speckle considering a phased array imaging technique. The third example represents the simulation of a cardiac image (the amplitudes of the scatterers were related to the gray levels of an Apical 4 Chambers (A4C) view image, as suggested in [27]). The experimental data was acquired with an Ultrasonix MDP research platform. The simulation and experimental parameters are resumed in Table 2.

For all the following examples, the improved version of MV BF was used, the one that gives the best results in [6], with spatial averaging with $L = M_{act}/2 = 32$, temporal averaging $T = 10$, and the diagonal loading factor $\Delta = 1/L$. The B-mode image computation was processed in a standard manner and in the same way for all the resulted images: Hilbert-based demodulation and logarithmic compression.

**Table 2**
Parameters of simulated and experimental images.

| Parameters for simulation of: | Point reflectors (Fig. 1) | Reflectors and cyst (Fig. 3) | Cardiac image (Fig. 6) | Experimental phantom (Fig. 8) |
|---|---|---|---|---|
| *Transducer* | | | | |
| Transducer type | Linear array | Phased array | Linear array | |
| Transducer element pitch (µm) | 475 | 132 | 231 | 118 |
| Transducer element kerf (µm) | 35 | 22 | 38.5 | 25 |
| Transducer element height (mm) | 5 | 5 | 14 | 4 |
| Central frequency, $f_0$ (MHz) | 3.5 | 7 | 4 | 7 |
| Sampling frequency, $f_s$ (MHz) | 100 | 60 | 40 | 40 |
| Speed of sound, $c$ (m/s) | 1540 | | | |
| Wavelength (µm) | 440 | 220 | 385 | 220 |
| Excitation pulse | Two-cycle sinusoidal at $f_0$ | | | |
| *Synthetic Aperture Emission* | | | | |
| Receive apodization | Hanning | | | |
| Number of transmitting elements | 64 | 128 | 64 | 128 |
| Number of receiving elements | 64 | 128 | 64 | 128 |
| Number of emissions | 129 | 128 | 204 | 192 |

### 4.1. Simulated point reflectors

A scanned grid with 14 point reflectors was simulated, laterally aligned in pairs of two and separated by 4 mm. They are located at axial depths ranging from 40 to 80 mm, with a transmit focus at 50 mm and a dynamic receive focalisation.

### 4.2. Simulated point reflectors and cyst data

For this type of simulation the medium was scanned with a 7 MHz 128-element phased array transducer with $wavelength/2$ spacing and Hanning apodization. A two-cycle sinusoidal was used as excitation and the transmit focus was set to 60 mm. We adopted a dynamically receive focalisation ranging from 5 to 150 mm. The images consist in 128 lines with 0.7° between consecutive lines. The medium consists in several circular cysts: an anechoic one with radius 2 mm, a hyperechoic one with radius 3 mm, an echoic one with radius 2 mm and one hypo-echoic with radius 1.5 mm. It also contains nine point reflectors situated at different positions. The scatterers are uniformly random distributed within the phantom cyst, and the scatterer amplitudes are Gaussian distributed with a standard deviation determined by the scatterer map, with the amplitude of the scatterers mapped to the intensity given through a bitmap image.

### 4.3. Simulated cardiac apical view image

The Apical 4 Chambers (A4C) view is a well exploited perspective in echocardiography, containing information about the left ventricle (LV) and right ventricle (RV) of the heart. A 3.75 MHz 64-elements transducer sectorial probe was used to obtain the simulated data which holds information about the LV, the scatterers having uniform random positions. The sampling frequency is 40 MHz, the view angle 66°, the transmit focus point is set to 65 mm, and a pitch equal with half of one wavelength is used to avoid grating lobes effects. The final image is ultra-realistic, the amplitudes being related to an in vivo cardiac image [27]. For both point reflectors with cyst data (Section 4.2) and cardiac image simulations, the number of scatterers was sufficiently large to produce fully developed speckle.

### 4.4. Recorded phantom data

The phantom data was recorded using the Ultrasonix MDP research platform equipped with the parallel channel acquisition system SonixDaq and the linear L14-W/60 Prosonic© (Korea) ultrasonic probe having 128 elements with height of 4 mm, sub-element width of 0.093 mm, and kerf of 0.025 mm. The central frequency is $f_0 = 7$ MHz and the sampling frequency is $f_s = 40$ MHz. The scanned medium is a general-purpose ultrasound phantom CIRS Model 054GS.

### 4.5. Image quality measures

Three conventional image quality metrics were calculated: the contrast ratio (CR) index, the contrast-to-noise ratio (CNR), and the signal-to-noise ratio (SNR). They were computed based on the envelope-detected signals independent of image display range. Recently, Rindal et al. showed in [9] that the improved contrast of MV beamformer is due to the improved edges, so dependent on the resolution improvement of the beamformed image. Moreover, they showed that for very small ROIs, DAS with Hamming apodization produces better contrast that MV. However, we will show that by the detection of the strong reflectors, the proposed method will considerably increase the contrast of the final image.

Based on the mean values in a region $R_1$ and a region $R_2$, CR is defined as [28]:

$$CR = |\mu_{R_1} - \mu_{R_2}|, \tag{16}$$

where $\mu_{R_1}$ and $\mu_{R_2}$ are the mean values in the region $R_1$, respectively $R_2$.

CNR is defined as [9]:

$$CNR = \frac{|\mu_{R_1} - \mu_{R_2}|}{\sqrt{\sigma_{R_1}^2 + \sigma_{R_2}^2}}, \tag{17}$$

where $\sigma_{R_1}$ and $\sigma_{R_2}$ are the standard deviations of intensities in $R_1$, respectively $R_2$.

The SNR is defined as the ratio between the mean value $\mu$ and the standard deviation $\sigma$ in homogeneous regions [12]:

$$SNR = \frac{\mu}{\sigma}. \tag{18}$$

## 5. Results and discussion

### 5.1. Sparsely located point reflectors

With this simulation we evaluated the potential of the proposed methods to precisely detect the strong reflectors in sparse mediums. The results prove that all the 14 sparsely located reflectors are detected at correct positions. The beamformed responses are illustrated in Fig. 1. One can observe that using DAS BF with a Hanning apodisation window (Fig. 1(a)) produces results with poor lateral resolution and high sidelobes. Although MV offers better resolution, the sidelobes are still remarkable, Fig. 1(b). Clearly, Fig. 1(c) and (d) present superiority over DAS and MV BF in terms of lowering the sidelobes of the final image. These results validate that USBIC and M-USBIC beamformers correctly detect the strong reflectors in a sparse medium. For a sparse medium USBIC and M-USBIC give a good approximation of the reflectors' position. $\lambda$ can range between 0.8 and 1 for a perfect detection of the number of reflectors. Since we are dealing with a sparse medium with no speckle, $\gamma$ was set to 0 for this result.

Note that, even if the amplitude of the response of the reflectors obtained with DAS is decreasing with depth (see Fig. 1(a)), the proposed method is able to detect the 14 reflectors placed at different depths. Contrarily, a simple thresholding method would firstly select the positions corresponding to the sidelobes of the first reflected echoes before selecting the positions corresponding to scatterers at higher depths.

In Fig. 2 we reinforce the conclusions related to the capability of the strong reflector based approaches to eliminate the sidelobes by drawing the lateral variation of the beamformed responses at axial depth of 50 mm (Fig. 2(a)) and 70 mm (Fig. 2(b)). We can clearly observe the ability of USBIC and M-USBIC to correctly detect the isolated scatterers, compared to the relatively large mainlobe and high sidelobes generated by standard beamforming techniques.

### 5.2. Point reflectors and cyst data

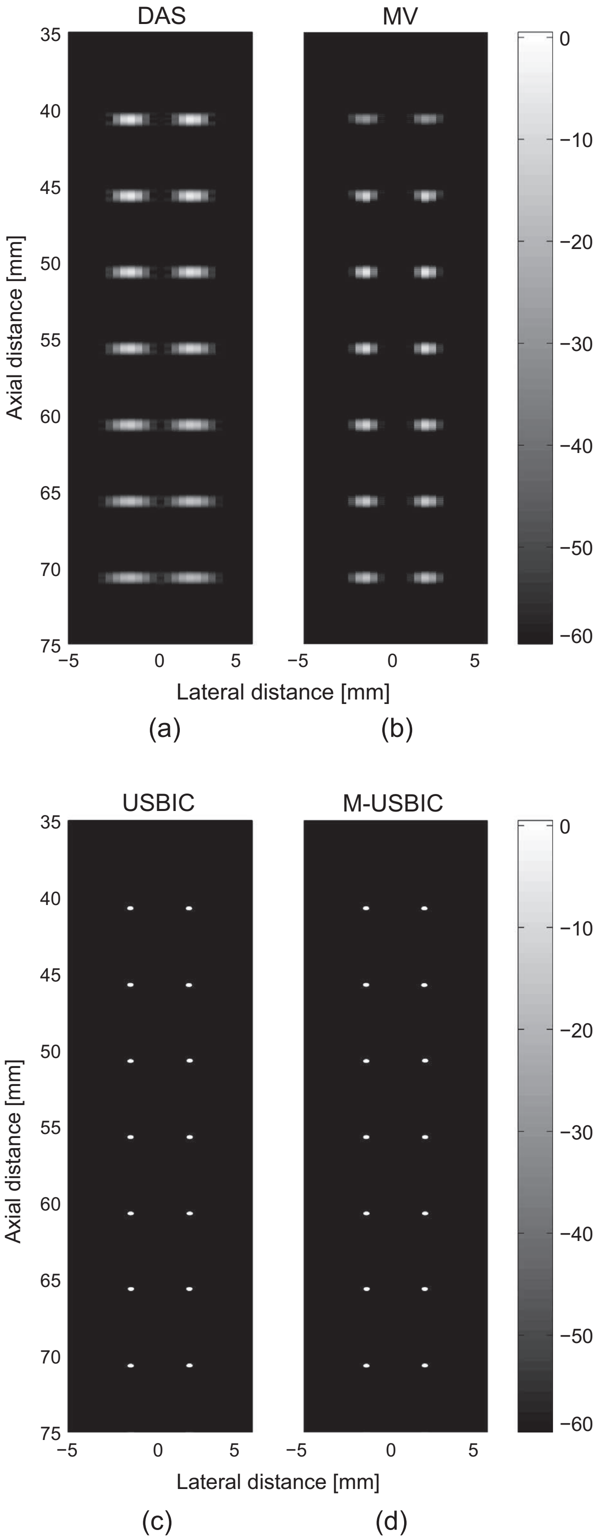

**Fig. 1.** (a) DAS, (b) MV, (c) USBIC, and (d) M-USBIC BF results of 14 sparsely located reflectors.

Fig. 3 presents the BF results of a simulated medium with the phased array imaging technique. The image quality metrics are detailed in Table 3. We calculate CR and CNR on anechoic and hyperechoic cysts (in Fig. 3(a), they are delimited by white circles). For both cases the $R_2$ regions are the black circles situated at the same depth with the bounded cysts, as suggested in [9]. For the calculation of the SNR, the ROIs are all the black encircled regions together with the gray surrounded region. The SNR was calculated for each region and the final value is the average of the three SNRs. As stated in [9], while the ROIs of the cysts are chosen exactly at the limit of the cysts (Fig. 3(a)), we are not greatly enhancing the contrast by using MV (Fig. 3(b)), compared with DAS. On the other hand, by using USBIC or M-USBIC BF, it is normal to have a decrease in CR and CNR in comparison with DAS and MV when dealing with the anechoic cyst, since their aim is to remove speckle in the final image. Besides, evaluated for hyperechoic cyst and compared with DAS, M-USBIC has an improvement of more than 10 dB and of 1.6 in CR, respectively CNR, Table 3. With USBIC we can maintain a good CR even for anechoic cyst, while increasing by more than 10 dB the CR of the hyperechoic cyst, Fig. 3(d). Moreover, the proposed methods provide a trade-off between increasing the contrast and maintaining the speckle in the beamformed images, producing a gain of 4 in SNR when using M-USBIC BF (Fig. 3(f)) and of 0.7 when using USBIC (Fig. 3(e)), in comparison with DAS. Varying the parameters $\lambda$ and $\gamma$ allows the control of the number of the strong reflectors and the speckle information in the final image. We need to precise that the results are not too sensitive to the choice of $\lambda$. A change with an order of 10 must be chosen in order to have some remarkable differences between the final results. However, the higher $\lambda$ is, the more the speckle will be eliminated. This can highly affect the final result, while the speckle contains important information by delimiting the anechoic cyst. As solutions, we can decrease the value of $\lambda$, or increase the value of $\gamma$, that represents the percentage in the final image of the level of speckle present in DAS (in the case of USBIC) or MV (in the case of M-USBIC) results. For this example, USBIC BF with $\lambda = 10$ and $\gamma = 0.5$, and M-USBIC BF with $\lambda = 70$ and $\gamma = 0.7$ perform the best results in terms of preserving the speckle while increasing the contrast of the final image.

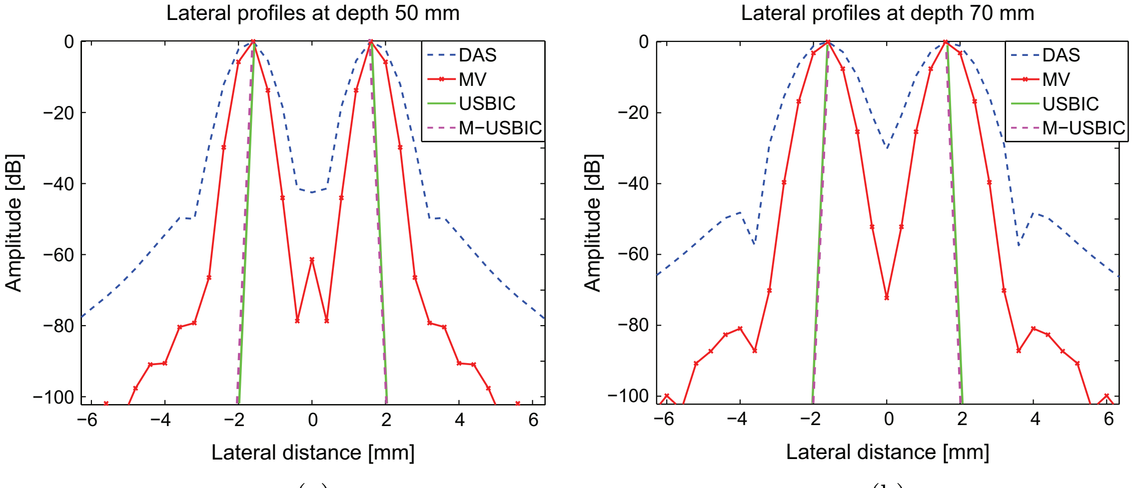

(a) (b)

**Fig. 2.** Lateral variations of the images from Fig. 1 at (a) depth 50 mm and (b) 70 mm.

The main issue of using a low $\gamma$ parameter is that the contrast of anechoic cysts tends to be attenuated with the decrease in $\gamma$. A simple way to overcome this issue is to choose $\gamma = \frac{1}{2}$ that is, to give the weight to each term in (14) and (15) which is a fair (and easy to achieve) compromise. For example, by adding the images in Fig. 3 (a) and (c) we obtain the result in Fig. 3(g). Similarly, by summing the images in Fig. 3(b) and (d) results into the image in Fig. 3(h). From Fig. 3(g) and (h) we can observe that the anechoic cyst is better defined compared with the results when the images obtained with USBIC and M-USBIC are weighted with $\gamma$. This observation is enforced by the results of CR, CNR and SNR from Table 3, where for USBIC ($\lambda = 10$) the values of CR and CNR for the anechoic cyst are very close to the ones for DAS image, while the SNR is improved. Moreover, the hyperechoic cyst has better contrast than DAS, but not so important as when using the weighting parameter $\gamma$ for computing the final result. Similar remarks can be formulated for M-USBIC ($\lambda = 70$) that preserves the low echoic region in the beamformed image. Thus, even if the aim of the proposed methods are to detect the strong reflectors present in the medium, if there exist anechoic structures, they can be preserved, by adding the speckle from the DAS or MV images to the USBIC, respectively M-USBIC results, without any weighting parameter $\gamma$.

The previous observations are enforced by Fig. 4, where the lateral profiles around the anechoic (Fig. 4(a)) and hyperechoic (Fig. 4 (b)) cysts are drawn. For this figure we considered USBIC with $\lambda = 10$ and $\gamma = 0.5$ (Fig. 3(e)), and M-USBIC with $\lambda = 70$ and $\gamma = 0.7$ (Fig. 3(f)). We can observe that the lateral profile when using USBIC is comparable with MV, and has wider mainlobe than DAS in the case of anychoic cyst's profile (Fig. 4(a)), while its propose is to eliminate speckle around the cyst. M-USBIC is eliminating even more the speckle, so the hyperechoic cyst will be enlarged. However, for anechoic cysts M-USBIC provides the narrower mainlobe, the cyst appearing more well defined in Fig. 3 (f). The lateral profiles when using USBIC and M-USBIC have lower average in amplitude, due to the fact that only one fraction $(1-\gamma)$ of the DAS and MV beamformed images are added to the image $\mathbf{S}$ (USBIC or M-USBIC), see (14) and (15).

Thus, we may remark that the main advantage of our method is to improve the contrast of hyperechoic structures, based on the detection of strong reflectors. However, by adding speckle to the final images, despite a reduction of this contrast gain, we manage to maintain a contrast of hypoechoic structures close to the one provided by existing beamforming techniques.

For this example, USBIC with $\lambda = 10$ corresponding to the image in Fig. 3(c), required 8783 iterations, that is equivalent to the number of the detected reflectors, while M-USBIC dissociated 1982 strong reflectors, when $\lambda = 70$ (corresponding to the result in Fig. 3(d)). The two plots corresponding to USBIC and M-USBIC for this case are drawn in Fig. 5. We have also depicted the case when M-USBIC is used with $\lambda = 10$, for comparing the impact of keeping the same value of $\lambda$ on the two methods. We can observe that for the same $\lambda$, M-USBIC tends to detect less strong reflectors (2050), dissociating better than USBIC the strong reflectors from the speckle. This is due to the increase in CR, CNR, and SNR of MV, compared with DAS. We also emphasize that the number of strong reflectors detected with M-USBIC only slightly decreases when $\lambda$ changes from 10 to 70.

### 5.3. *Cardiac apical view image*

The results of beamforming on a simulated A4C view cardiac medium are illustrated in Fig. 6. To compute CR and CNR, $R_1$ was defined as the region inside the white rectangle around the position 58 mm (axial) and $-10$ mm (lateral) from Fig. 6(a) together with the $R_2$ (the region inside the white rectangle around 8 mm (axial), situated at the same depth as $R1$). For SNR, the regions surrounded by the black rectangles were chosen. The SNR was calculated according to (18) for each region and the average value was extracted. Table 4 lists the CR, CNR, and SNR values for each BF method.

In coherence with the conclusions stated in [9], MV does not exhibit a higher contrast than DAS when selecting a small ROI, see Table 4. Contrarily, we obtain an improvement in CR of more than 20 dB with USBIC and M-USBIC, compared with DAS and MV, Fig. 6(c) and (d). Of course, in these situations, due to the elimination of the level of speckle, the SNR is much smaller than for DAS and MV. Our empirical experience shows that a value of $\lambda \approx 50$ is optimal in terms of contrast and visual perception of the resulted beamformed image when we use USBIC BF approach (Fig. 6(e)), and a value of $\lambda \approx 25$ for M-USBIC BF (Fig. 6(f)). When dealing with a non-sparse medium, $\gamma$ is an important parameter that regulates the appearance of the final image, by controlling the level of speckle. A value of $\gamma = 0$ will result in an image with almost no speckle, Fig. 6(c) and (d). A small value of $\gamma$ is sufficient for obtaining a trade-off between the contrast enhancement and retain of speckle information in final image. As $\gamma$ increases, the

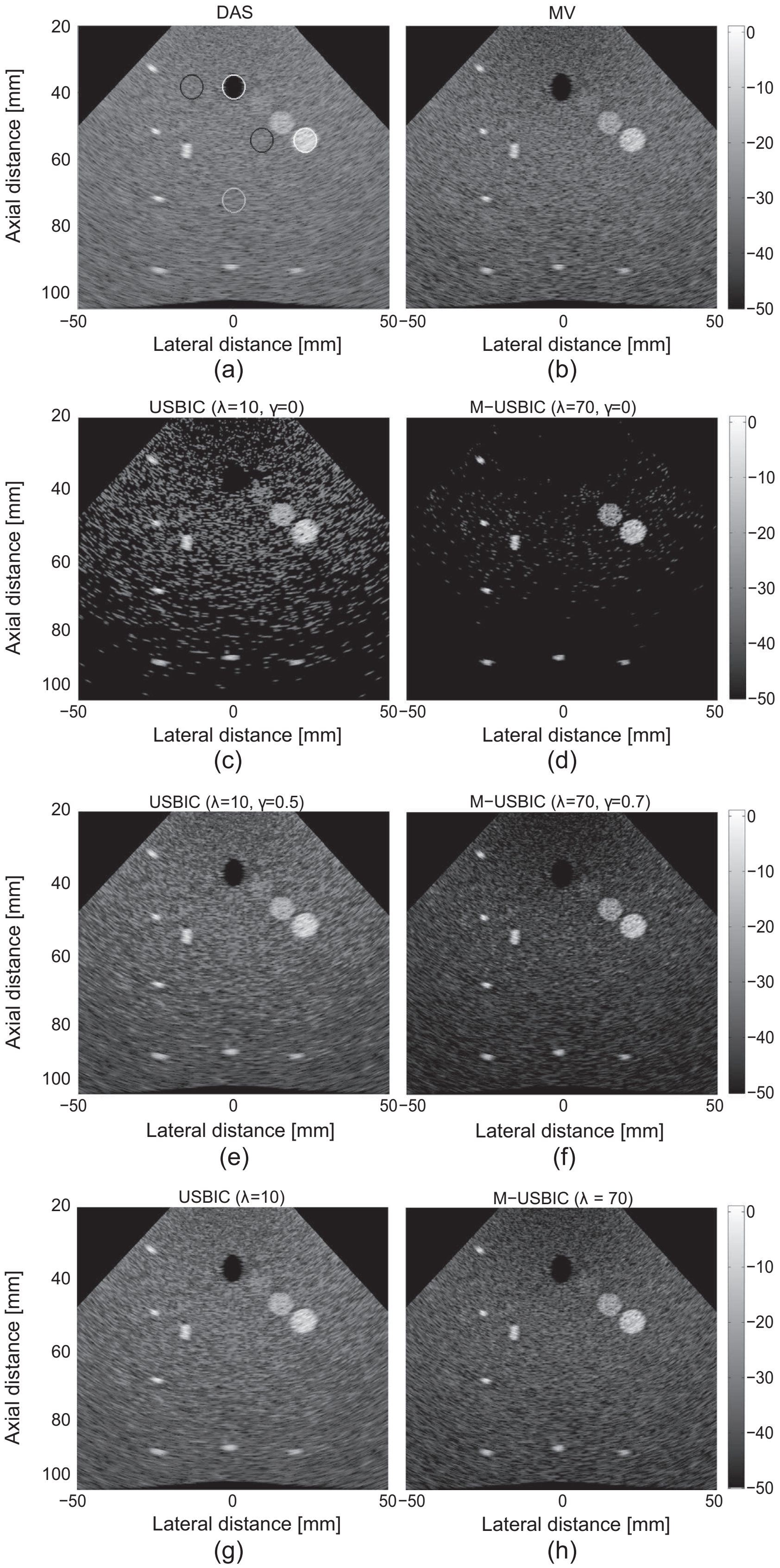

**Fig. 3.** Results of (a) DAS, (b) MV, (c) USBIC with $\lambda = 10$, and $\gamma = 0$, (d) M-USBIC with $\lambda = 70$ and $\gamma = 0$, (e) USBIC with $\lambda = 10,\ \gamma = 0.5$, and (f) M-USBIC with $\lambda = 70$ and $\gamma = 0.7$, (g) USBIC with $\lambda = 10$, and (h) M-USBIC with $\lambda = 70$ on a simulated medium using the phased array imaging technique. The image quality metrics: CR, CNR, and SNR are given in Table 3.

**Table 3**
CR, CNR and SNR values of the beamformed images using the simulated point reflectors and cyst data medium, Fig. 3.

| BF method | Anechoic cyst | | Hyperechoic cyst | | Black-circle region |
|---|---|---|---|---|---|
| | CR (dB) | CNR | CR (dB) | CNR | SNR |
| DAS | 29.785 | 5.120 | 33.703 | 2.621 | 3.061 |
| MV | 21.953 | 5.290 | 34.712 | 2.980 | 3.770 |
| USBIC ($\lambda = 10, \gamma = 0$) | 10.469 | 3.710 | 47.586 | 4.233 | 3.912 |
| USBIC ($\lambda = 10, \gamma = 0.5$) | 23.391 | 5.315 | 39.634 | 3.281 | 3.701 |
| USBIC ($\lambda = 10$) | 25.223 | 5.273 | 38.052 | 3.082 | 3.570 |
| M-USBIC ($\lambda = 10, \gamma = 0$) | 0.185 | 0.693 | 54.320 | 5.557 | 6.365 |
| M-USBIC ($\lambda = 70, \gamma = 0.7$) | 8.875 | 4.943 | 45.435 | 4.348 | 7.042 |
| M-USBIC ($\lambda = 70$) | 15.102 | 5.213 | 40.524 | 3.702 | 5.044 |

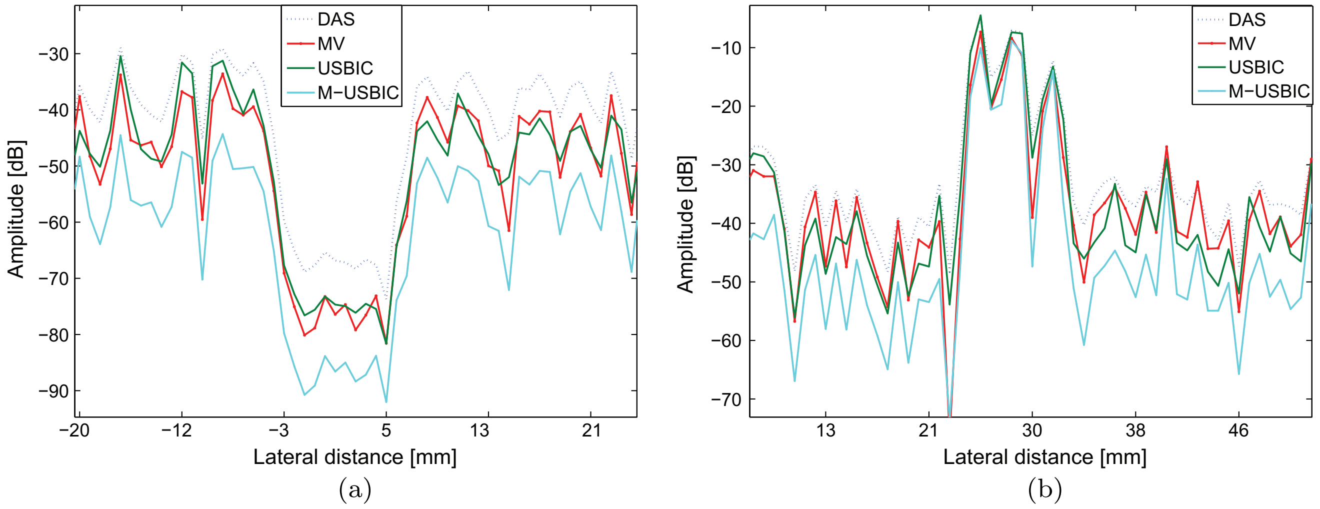

**Fig. 4.** Lateral profiles of the images from Fig. 3. (a) The lateral profile at the axial depth of 40 mm, that intersects the anechoic cyst. (b) The lateral profile at the axial depth of 70 mm, that intersects the hyperchoic cyst. The lateral profiles were drawn considering USBIC with $\lambda = 10$ and $\gamma = 0.5$ (Fig. 3(e)), and M-USBIC with $\lambda = 70$ and $\gamma = 0.7$ (Fig. 3(f)).

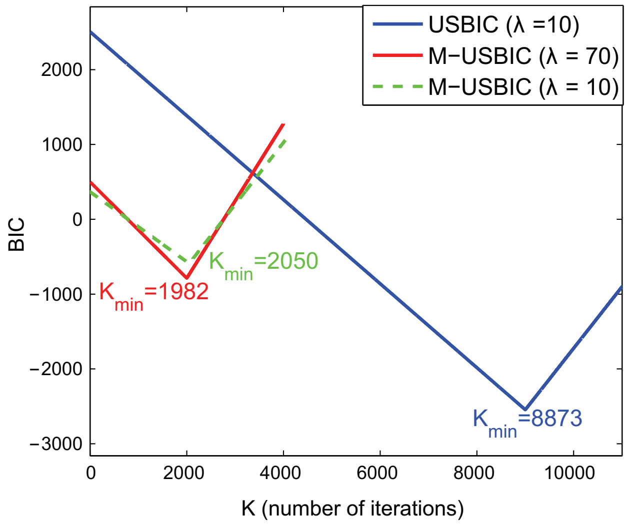

**Fig. 5.** Values of BIC versus K for USBIC with $\lambda = 10$ and $\gamma = 0$ (Fig. 3(c)) and M-USBIC with $\lambda = 70$ and $\gamma = 0$ (Fig. 3(d)).

contrast of the image is getting closer to the values of DAS, or MV beamformed images. For this simulated medium, the choice of the parameters was influenced on offering continuity of the ventricle structures, while increasing as much as possible the contrast of the final image. USBIC BF achieve the best results with $\lambda = 50$ and $\gamma = 0.5$, while for M-USBIC we obtained the best outcome with $\lambda = 25$ and $\gamma = 0.5$.

In practical situations, the choice of the hyperparameters $\lambda$ and $\gamma$ may be a difficult task. When dealing with optimization problems, the parameter $\lambda$ is usually employed, to balance between the prior information of the strong reflectors and the data fidelity. We may remark that in most of the optimization problems such a hyperparameter is employed. See for example the well-known Least Absolute Shrinkage and Selection Operator (LASSO) problem [29], where such a parameter balances between the $\ell_1$ and $\ell_2$ norms or algorithms such as Orthogonal Matching Pursuit (OMP) [30] (similar to our approach in the sense of the idea of minimizing a $\ell_0$ pseudo norm) where the stop criterion is either the pre-defined number of atoms or the value of the residuals.

On the other hand, the choice of $\gamma$ may depend on the application and on the necessity of visualizing the speckle noise in homogeneous regions or not. Its values are in the range $[0, 1]$, where for 0, no influence of the beamformed data is added to the final result, while for 1 all the speckle information from the beamformed data is added to the final result. Fig. 7 shows how the parameters $\lambda$ and $\gamma$ influence the values of CNR and SNR of the beamformed image in the case of USBIC (Fig. 7(a) and (b)) and M-USBIC (Fig. 7(c) and (d)). As expected, we can observe that $\gamma$ has a great influence on SNR, that is increasing with the value of $\gamma$. This is related to the fact that

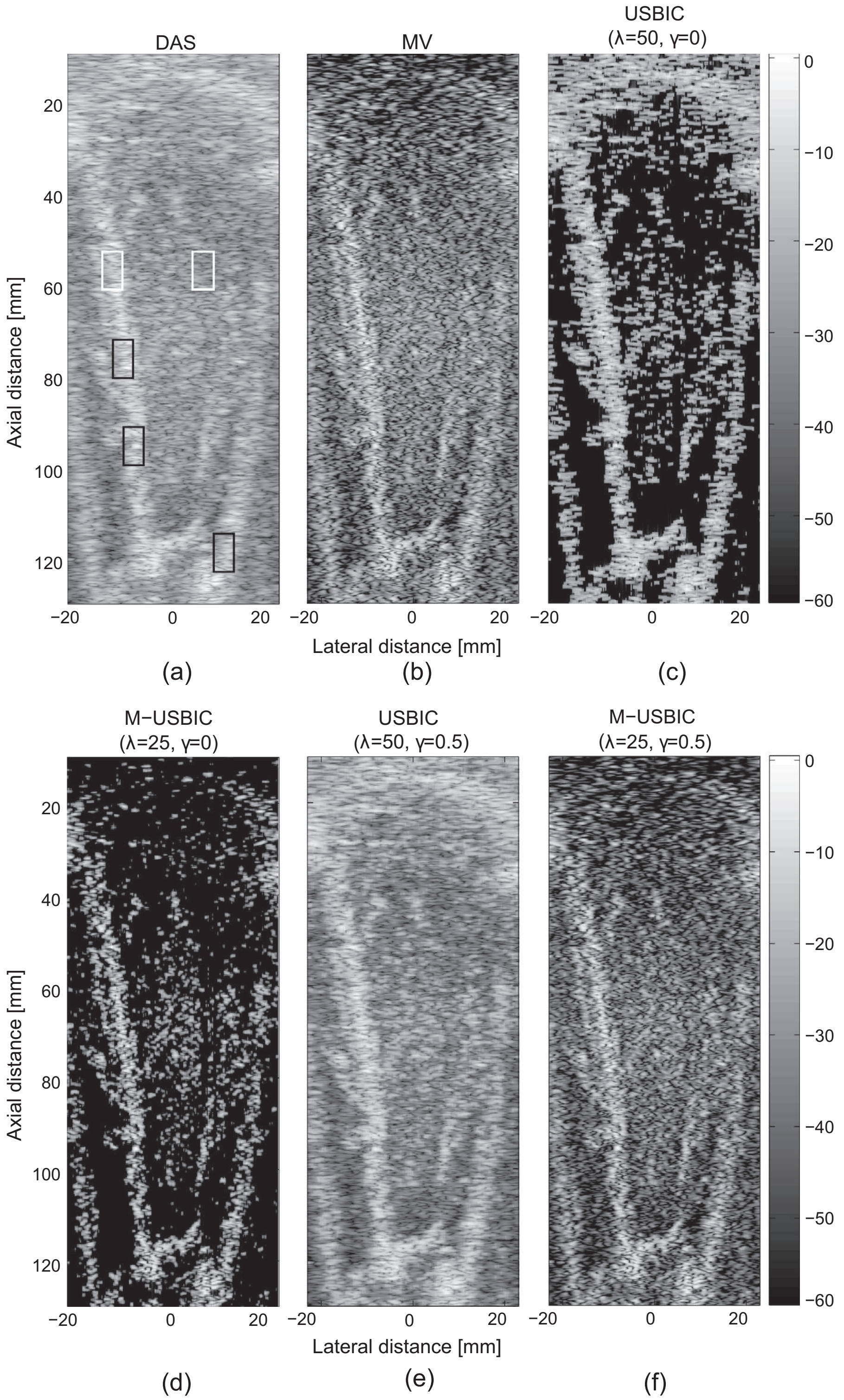

**Fig. 6.** Results of (a) DAS, (b) MV, (c) USBIC with $\lambda = 50$, and $\gamma = 0$, (d) M-USBIC with $\lambda = 25$ and $\gamma = 0$, (e) USBIC with $\lambda = 50$, and $\gamma = 0.5$, and (f) M-USBIC with $\lambda = 25$ and $\gamma = 0.5$ on a simulated cardiac apical view image. The image quality metrics: CR, CNR, and SNR are given in Table 4. In (a) we marked the regions used for the calculation of CR, CNR, and SNR.

$\gamma$ is influencing the level of speckle in the final image, by adding to the USBIC or M-USBIC beamformed image a percentage of the DAS or MV beamformed image, as discussed in Section 3.3. One can observe that the value of speckle is on one hand influenced by the $l_2$-norm data fidelity term and on the other hand, by the hyper-parameters $\lambda$ and $\gamma$. However, the parameter $\lambda$ has further impact on the value of CNR. For example, when applying USBIC BF, a value of $\lambda = 50$ and a low $\gamma$ results in a maximum of CNR, while for the other values of $\lambda$, the CNR degrades, see Fig. 7(a). This is not true in the case of M-USBIC, where the influence of $\gamma$ is more important that the one of $\lambda$, Fig. 7(c). This is due to initial decrease of the level of speckle when applying MV BF.

**Table 4**
CR, CNR and SNR values of the beamformed images using the simulated cardiac apical view medium, Fig. 6.

| BF method | CR (dB) | CNR | SNR |
|---|---|---|---|
| DAS | 10.938 | 1.209 | 1.285 |
| MV | 10.366 | 0.663 | 0.609 |
| USBIC ($\lambda = 50, \gamma = 0$) | 35.210 | 1.478 | 0.321 |
| USBIC ($\lambda = 50, \gamma = 0.5$) | 14.975 | 1.475 | 1.055 |
| M-USBIC ($\lambda = 25, \gamma = 0$) | 33.110 | 1.092 | 0.272 |
| M-USBIC ($\lambda = 25, \gamma = 0.5$) | 12.283 | 0.733 | 0.569 |

### *5.4. Recorded experimental data*

Applied on experimental data, the results of the aforementioned BF methods are illustrated in Fig. 8. To calculate CR and CNR, $R_1$ is represented in the region surrounded by the white ellipse in Fig. 8(a) and $R_2$ is inside the black ellipse situated at the same depth as $R_1$. The three black ellipses from Fig. 8(a) indicate the regions used to calculate the SNR. For each ellipse its corresponding SNR is calculated, the final SNR value being calculated as the average of the three values of SNR. The values of CNR and SNR for this example are resumed in Table 5. Indeed, the small contrast improvement (of 0.1 dB, compared with DAS) in the case of MV may be due to the gain in resolution as stated in [9], the level of speckle, measured by SNR, decrease. On the other hand, when using MV BF (Fig. 8(b)) the point-like structures are much well defined. We can observe that the tendency of the proposed method on the experimental data is to eliminate the speckle from higher depths, (Fig. 8(c) and (d)). As consequence, we need a relatively high value of $\gamma$ in order to ensure continuity in the final image ($\gamma = 0.7$), as in Fig. 8(e) and (f). Moreover, by increasing $\lambda$ we can achieve better SNR while preserving a good contrast. In the case of USBIC, the beamformed image with the best trade-off between contrast and

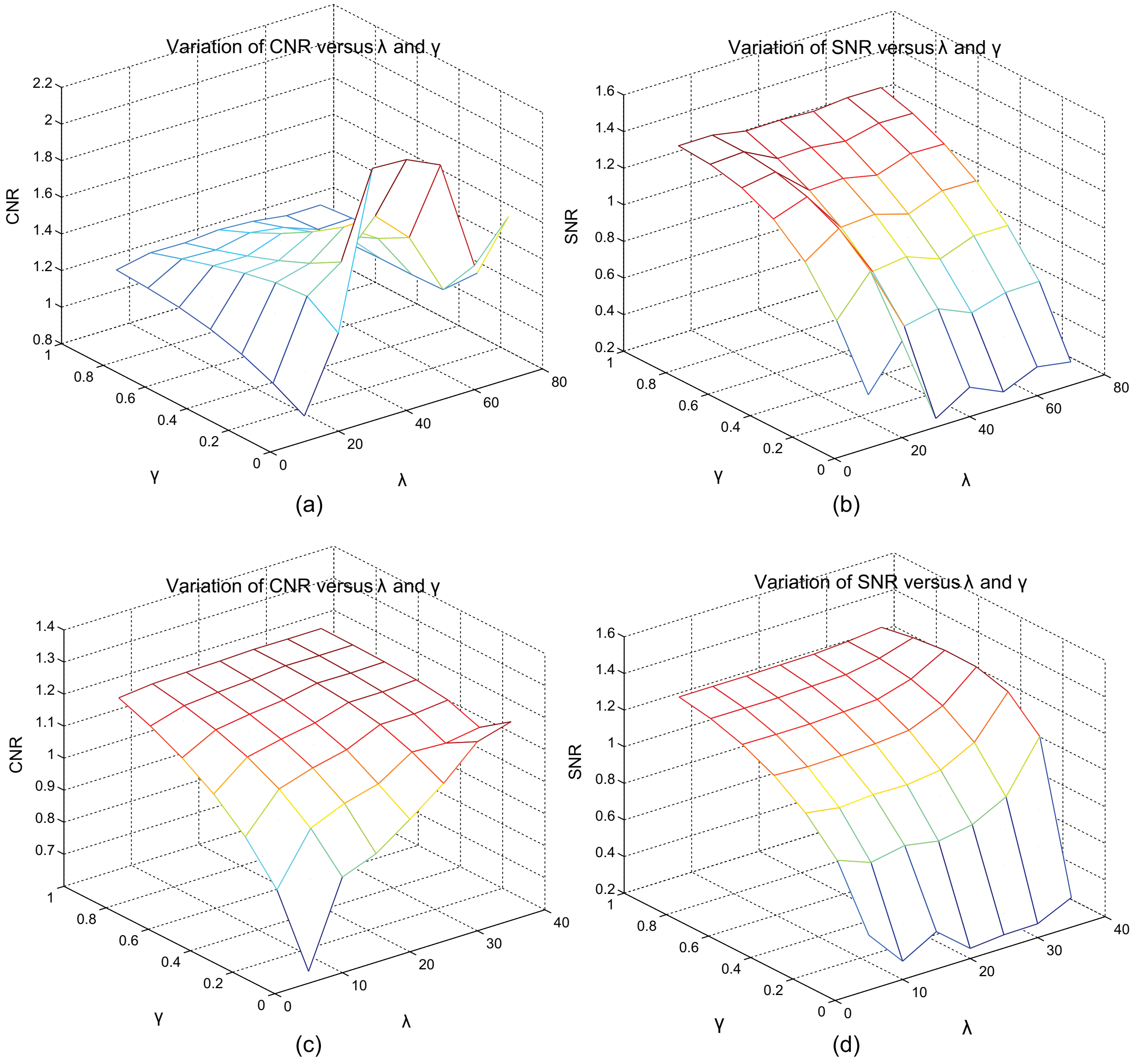

**Fig. 7.** The variation of the CNR and SNR versus the parameters $\lambda$ and $\gamma$ when USBIC BF method (a and b), and M-USBIC BF method (c and d) are applied to the cardiac view simulation detailed in Section 4.3.

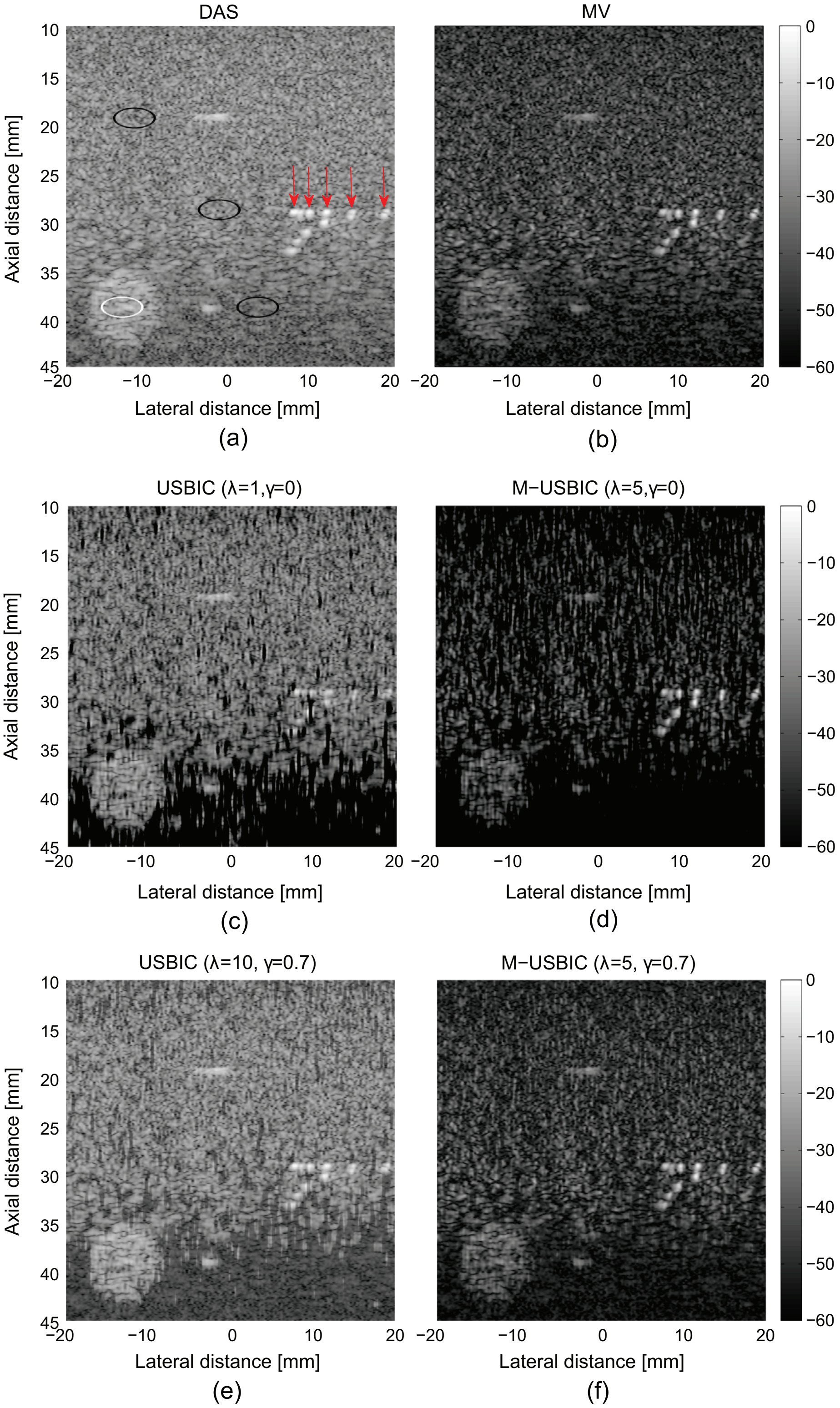

**Fig. 8.** Results of (a) DAS, (b) MV, (c) USBIC with $\lambda = 1$, and $\gamma = 0$, (d) M-USBIC with $\lambda = 5$ and $\gamma = 0$, (e) USBIC with $\lambda = 10$, and $\gamma = 0.7$, and (f) M-USBIC with $\lambda = 5$ and $\gamma = 0.7$ on recorded experimental data. The image quality metrics: CR, CNR and SNR are given in Table 5. In (a) we marked the regions used for the calculation of CR, CNR and SNR.

speckle preservation was obtained with $\lambda = 10$ and $\gamma = 0.7$, while M-USBIC performed better when $\lambda = 5$ and $\gamma = 0.7$.

For enforcing the previous observations, the lateral profiles are provided in Fig. 9. We considered the case of USBIC with $\lambda = 10$ and $\gamma = 0.7$ (Fig. 8(e)), and of M-USBIC with $\lambda = 5$ and $\gamma = 0.7$ (Fig. 8(f)). In the case of the lateral profile that intersects the point-like reflectors, Fig. 9(a), we can observe that for MV and M-USBIC the scatterers are well separated, M-USBIC eliminating as much as possible

**Table 5**
CR, CNR and SNR values of the beamformed images by using the recorded experimental data, Fig. 8.

| BF method | CR (dB) | CNR | SNR |
|---|---|---|---|
| DAS | 3.532 | 1.602 | 9.745 |
| MV | 3.641 | 1.085 | 6.443 |
| USBIC ($\lambda = 1, \gamma = 0$) | 6.448 | 1.943 | 7.258 |
| USBIC ($\lambda = 10, \gamma = 0.7$) | 5.034 | 1.952 | 8.702 |
| M-USBIC ($\lambda = 5, \gamma = 0$) | 4.013 | 1 | 5.408 |
| M-USBIC ($\lambda = 5, \gamma = 0.7$) | 4.105 | 1.745 | 9.434 |

the speckle around them. By using the proposed BF method it is possible to distinguish five point-reflectors (indicated by red arrows), while this is less evident in the case of DAS and USBIC. In Fig. 9(b), the profile related to the massive cyst is more narrow than for DAS, MV and USBIC, so just the strongest reflectors inside the cyst are kept.

Even if we are able to highly improve the contrast of the final image by reinforcing the strong reflectors, the main advantage of DAS and MV over USBIC and M-USBIC is the computational time in the case when the scanned medium is not sparse, since the number of the iterations of the proposed methods increases directly with the number of the strong reflectors inside the medium. For example, to obtain the beamformed images from Fig. 1, we directly applied the 2D refinement process (USBIC) to the beamformed DAS image, as described in Section 3.2.2, and we obtained a computational time roughly two times lower than MV BF. The obtained values are given in Table 6. However, when more complex mediums are scanned, the 1D initialization process, that is detecting the strong reflectors RF line by RF line, needs to be added to speed up the 2D refinement step. The 1D initialization, described in Section 3.2.1, can be even 10 times longer than MV. However, since it is processed line by line, standard parallel computing methods could highly reduce the computational complexity. The 2D refinement method is comparable in time of computation with the MV BF. The computational time values for obtaining the beamformed images from Fig. 8 are given in Table 6, for the case of USBIC beamformer, and are obtained without using any parallel computing. All the discussed methods were implemented with Matlab R2013b, on an Intel i7 2600 CPU working at 3.40 GHz.

**Table 6**
Computational time required to beamform the images in Figs. 1 and 8.

| BF method | Computational time (min) | |
|---|---|---|
| | Fig. 1 | Fig. 8 |
| DAS | 0.075 | 0.215 |
| MV | 5.124 | 10.272 |
| 1D initialization | – | 72.763 |
| USBIC | 1.725 | 13.532 |

## 6. Conclusions

In this paper we proposed a beamforming approach based on the detection of the strong reflectors in US imaging. We validate the precision of the detection of the number and the position of the reflectors in a sparse medium, and we evaluate the proposed methods (USBIC and M-USBIC) on different types of simulated data and on experimental data. For a less sparse medium, the $\lambda$ parameter is deciding the sparsity level in the final beamformed image. Our empirical experience suggests that it can be set between large intervals in a non-sparse medium. For example, by increasing the value of $\lambda$ by a factor of 5, we favor the sparsity in the resulted image. After deciding the best $\lambda$ in function of the desired experiment, the other parameter, $\gamma$ will set the level the speckle in the final image. For non-sparse mediums, a value of $\gamma$ in the interval 0.5–0.8 offers the most coherent results, while enhancing the detected reflectors in the final image. Hence, the strong reflector based BF methods allow region differentiation (for example blood vessels, or cysts), while preserving speckle statistics that often contain important clinical information. The main disadvantage of the proposed methods is the high computational cost when dealing with highly non-sparse scanning mediums. We should remark that the most computational expensive step is the 1D detection of the strong reflectors. However, this step may be largely fasten by parallelly processing the RF lines. The automatic choice of the hyper-parameters such as the one balancing between the data fidelity term and the sparsity of the strong reflectors, based for example on existing cross-validation techniques such as [24,25], is also a very interesting research track. Finally, the proposed approach may be improved by the use of sparse prior in appropriate bases, other than the direct strong reflection domain.

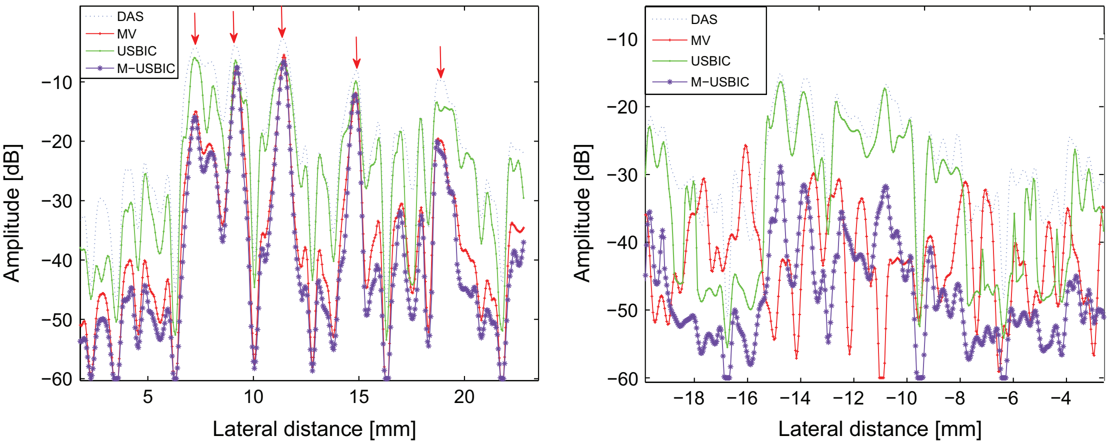

(a) (b)

**Fig. 9.** Lateral profiles of the images from Fig. 8. (a) The lateral profile at the axial depth of 28 mm, that intersects the point reflectors. The red arrows correspond to the point-like reflectors indicated in Fig. 8(a) by red arrows. (b) The lateral profile at the axial depth of 40 mm, that intersects the massive cyst. We considered the case of USBIC with $\lambda = 10$ and $\gamma = 0.7$ (Fig. 8(e)), and of M-USBIC with $\lambda = 5$ and $\gamma = 0.7$ (Fig. 8(f)). (For interpretation of the references to color in this figure legend, the reader is referred to the web version of this article.)

## Acknowledgements

We wish to thank Adeline Bernard and Hervé Liebgott, from CREATIS laboratory, University of Lyon, for providing the experimental ultrasound phantom data. This work was partially supported by ANR-11-LABX-0040-CIMI within the program ANR-11-IDEX-0002-02 of the University of Toulouse.

## References

[1] B.D. Van Veen, K.M. Buckley, Beamforming: a versatile approach to spatial filtering, IEEE ASSP Mag. 5 (2) (1988) 4–24.
[2] J. Capon, High-resolution frequency-wavenumber spectrum analysis, Proc. IEEE 57 (8) (1969) 1408–1418.
[3] K.L. Bell, Y. Ephraim, H.L. Van Trees, A bayesian approach to robust adaptive beamforming, IEEE Trans. Signal Process. 48 (2) (2000) 386–398.
[4] J. Li, P. Stoica, Z. Wang, On robust capon beamforming and diagonal loading, IEEE Trans. Signal Process. 51 (7) (2003) 1702–1715.
[5] B.M. Asl, A. Mahloojifar, A low-complexity adaptive beamformer for ultrasound imaging using structured covariance matrix, IEEE Trans. Ultrason. Ferroelectr. Freq. Control 59 (4) (2012) 660–667.
[6] B.M. Asl, A. Mahloojifar, Minimum variance beamforming combined with adaptive coherence weighting applied to medical ultrasound imaging, IEEE Trans. Ultrason. Ferroelectr. Freq. Control 56 (9) (2009) 1923–1931.
[7] I.K. Holfort, F. Gran, J.A. Jensen, Broadband minimum variance beamforming for ultrasound imaging, IEEE Trans. Ultrason. Ferroelectr. Freq. Control 56 (2) (2009) 314–325.
[8] K. Diamantis, I.K. Holfort-Voxen, A.H. Greenaway, T. Anderson, J.A. Jensen, V. Sboros, A comparison between temporal and subband minimum variance adaptive beamforming, in: SPIE Medical Imaging, International Society for Optics and Photonics, 2014, pp. 90400L–90400L.
[9] O.M.H. Rindal, J.P. Asen, S. Holm, A. Austeng, Understanding contrast improvements from capon beamforming, in: Ultrasonics Symposium (IUS), 2014 IEEE International, IEEE, 2014, pp. 1694–1697.
[10] T. Yardibi, J. Li, P. Stoica, Nonparametric and sparse signal representations in array processing via iterative adaptive approaches, in: 42nd Asilomar Conference on Signals, Systems and Computers, 2008, IEEE, 2008, pp. 278–282.
[11] T. Yardibi, J. Li, P. Stoica, M. Xue, A.B. Baggeroer, Source localization and sensing: a nonparametric iterative adaptive approach based on weighted least squares, IEEE Trans. Aerosp. Electron. Syst. 46 (1) (2010) 425–443.
[12] A.C. Jensen, Austeng, The iterative adaptive approach in medical ultrasound imaging, IEEE Trans. Ultrason. Ferroelectr. Freq. Control 61 (10) (2014) 1688–1697.
[13] C. Quinsac, A. Basarab, J. Girault, D. Kouamé, Compressed sensing of ultrasound images: sampling of spatial and frequency domains, in: 2010 IEEE Workshop on Signal Processing Systems (SIPS), IEEE, 2010, pp. 231–236.
[14] R. Tur, Y.C. Eldar, Z. Friedman, Innovation rate sampling of pulse streams with application to ultrasound imaging, IEEE Trans. Signal Process. 59 (4) (2011) 1827–1842.
[15] N. Wagner, Y.C. Eldar, Z. Friedman, Compressed beamforming in ultrasound imaging, IEEE Trans. Signal Process. 60 (9) (2012) 4643–4657.
[16] T. Szasz, A. Basarab, M.-F. Vaida, D. Kouamé, Beamforming with sparse prior in ultrasound medical imaging, in: Ultrasonics Symposium (IUS), 2014 IEEE International, IEEE, 2014, pp. 1077–1080.
[17] J. Li, P. Stoica, Robust Adaptive Beamforming, Wiley Online Library, 2006.
[18] J.-F. Synnevag, A. Austeng, S. Holm, Adaptive beamforming applied to medical ultrasound imaging, IEEE Trans. Ultrason. Ferroelectr. Freq. Control, 54 (8) (2007) 1606–1613.
[19] J.-F. Synnevag, C.-I. Nilsen, S. Holm, P2b-13 speckle statistics in adaptive beamforming, in: Ultrasonics Symposium, 2007. IEEE, IEEE, 2007, pp. 1545–1548.
[20] J.-F. Synnevag, A. Austeng, S. Holm, Benefits of minimum-variance beamforming in medical ultrasound imaging, IEEE Trans. Ultrason. Ferroelectr. Freq. Control 56 (9) (2009) 1868–1879.
[21] S. Konishi, G. Kitagawa, Information Criteria and Statistical Modeling, Springer Science & Business Media, 2008.
[22] E.J. Candes, M.B. Wakin, S.P. Boyd, Enhancing sparsity by reweighted $\ell 1$ minimization, J. Fourier Anal. Appl. 14 (5–6) (2008) 877–905.
[23] N. Dobigeon, A. Basarab, D. Kouamé, J.-Y. Tourneret, Regularized bayesian compressed sensing in ultrasound imaging, in: 2012 Proceedings of the 20th European Signal Processing Conference (EUSIPCO), IEEE, 2012, pp. 2600–2604.
[24] N.P. Galatsanos, A.K. Katsaggelos, Methods for choosing the regularization parameter and estimating the noise variance in image restoration and their relation, IEEE Trans. Image Process. 1 (3) (1992) 322–336.
[25] S. Ramani, Z. Liu, J. Rosen, J. Nielsen, J.A. Fessler, Regularization parameter selection for nonlinear iterative image restoration and MRI reconstruction using GCV and SURE-based methods, IEEE Trans. Image Process. 21 (8) (2012) 3659–3672.
[26] J.A. Jensen, N.B. Svendsen, Calculation of pressure fields from arbitrarily shaped, apodized, and excited ultrasound transducers, IEEE Trans. Ultrason. Ferroelectr. Freq. Control 39 (2) (1992) 262–267.
[27] M. Alessandrini, H. Liebgott, D. Friboulet, O. Bernard, Simulation of realistic echocardiographic sequences for ground-truth validation of motion estimation, in: 19th IEEE International Conference on Image Processing (ICIP), 2012, IEEE, 2012, pp. 2329–2332.
[28] M. Xu, X. Yang, M. Ding, M. Yuchi, Spatio-temporally smoothed coherence factor for ultrasound imaging [correspondence], IEEE Trans. Ultrason. Ferroelectr. Freq. Control 61 (1) (2014) 182–190.
[29] R. Tibshirani, Regression shrinkage and selection via the lasso, J. Roy. Stat. Soc. Ser. B (Methodological) (1996) 267–288.
[30] J.A. Tropp, A.C. Gilbert, Signal recovery from random measurements via orthogonal matching pursuit, IEEE Trans. Inf. Theory 53 (12) (2007) 4655–4666.